Electronic Supplementary Material

Nonreciprocal coherent coupling of nanomagnets by exchange spin waves

Hanchen Wang[1,§], Jilei Chen[1,§], Tao Yu[2,§], Chuanpu Liu[1,§], Chenyang Guo[3,§], Song Liu[4,§], Ka Shen[5,§], Hao Jia[4,§], Tao Liu[6], Jianyu Zhang[1], Marco A. Cabero Z[4,1], Qiuming Song[4], Sa Tu[1], Mingzhong Wu[6], Xiufeng Han[3], Ke Xia[4], Dapeng Yu[4], Gerrit E. W. Bauer[7,8,9], and Haiming Yu[1] (✉)

[1] *Fert Beijing Institute, School of Integrated Circuit Science and Engineering, Beijing Advanced Innovation Center for Big Data and Brain Computing, Beihang University, Beijing 100191, China*
[2] *Max Planck Institute for the Structure and Dynamics of Matter, 22761 Hamburg, Germany*
[3] *Beijing National Laboratory for Condensed Matter Physics, Institute of Physics, University of Chinese Academy of Sciences, Chinese Academy of Sciences, Beijing 100190, China*
[4] *Shenzhen Institute for Quantum Science and Engineering (SIQSE), and Department of Physics, Southern University of Science and Technology (SUSTech), Shenzhen 518055, China*
[5] *Department of Physics, Beijing Normal University, Beijing 100875, China*
[6] *Department of Physics, Colorado State University, Fort Collins, Colorado 80523, USA*
[7] *Kavli Institute of Nanoscience, Delft University of Technology, 2628 CJ Delft, The Netherlands*
[8] *Institute for Materials Research, WPI-AIMR and CSNR, Tohoku University, Sendai 980-8577, Japan*
[9] *Zernike Institute for Advanced Materials, University of Groningen, Groningen, Nijenborgh 4, 9747 AG Groningen, The Netherlands*
[§] *Hanchen Wang, Jilei Chen, Tao Yu, Chuanpu Liu, Chenyang Guo, Song Liu, Ka Shen and Hao Jia contributed equally to this work.*

Supporting information to https://doi.org/10.1007/s12274-020-3251-5

Material characterization

The 20 nm-thick yttrium iron garnet film (YIG) on GGG substrate is grown by magnetron sputtering at room temperature. Before growing, the system has a base pressure of 1.0×10^{-8} Torr. During the sputtering, the argon pressure is 10 mTorr, the argon flow rate is 4 sccm and the power is fixed at 75 W. Immediately, after the sputtering, the films are annealed at 750 °C or 800 °C for 4 h in 1.12 Torr oxygen. The surface roughness is measured by the atomic force microscope (AFM) as shown in Fig. S1(a), the size of the presented region is 5 μm × 5 μm. The ferromagnetic resonance (FMR) power absorption spectra provide the high-frequency performance and the linewidth of the YIG films. As present in Fig. S1(b), the frequency is fixed at 17 GHz, one can extract the linewidth at this frequency is about $\mu_0\Delta H = 0.84$ mT through the Lorentz fitting, and for the frequency at 13 GHz, the extracted linewidth is about $\mu_0\Delta H = 0.82$ mT. The Gilbert damping α fitted by $\mu_0\Delta H = \frac{2}{\sqrt{3}\gamma}\alpha f + \mu_0 H_0$ is about 8×10^{-5}, and $\mu_0 H_0 = 0.73$ mT is the film inhomogeneity broadening. After changing the measurement frequency, the FMR dispersion is extracted from the measurement results and showing in Fig. S1(c), from which the saturation magnetization $\mu_0 M_S$ is extracted as 0.18 T.

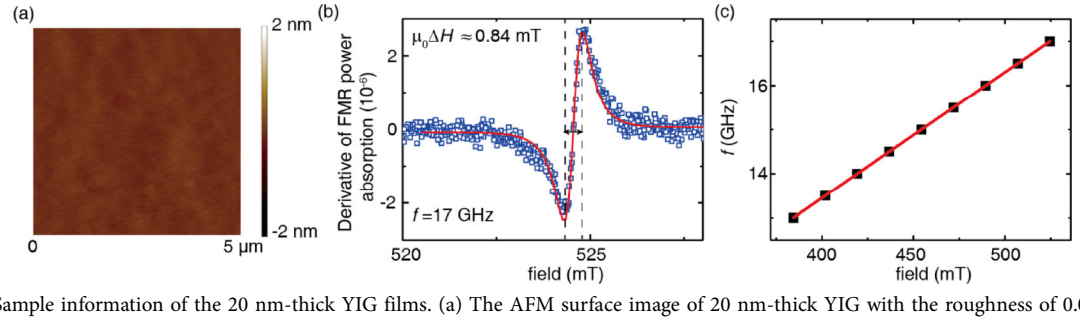

Figure S1 Sample information of the 20 nm-thick YIG films. (a) The AFM surface image of 20 nm-thick YIG with the roughness of 0.07 nm. (b) By using the Lorentz fitting of the FMR power absorption spectrum at 17 GHz, the linewidth $\mu_0\Delta H$ is about 0.84 mT. (c) The FMR frequency as a function of field, from which we extract the saturation magnetization $\mu_0 M_S = 0.18$ T.

Address correspondence to haiming.yu@buaa.edu.cn

Exchange spin waves with wavelength down to 48 nm and transmission spectra on other devices

Here, we present the transmission measurement results on other widths Co nanowire samples, namely, 50 nm (Fig. S2(b)) and 70 nm wide (Fig. S2(a)). In our measurement, the shortest wavelength spin waves is observed in the measurement results of the narrowest (50 nm-wide) sample corresponding to the highest frequency of Co FMR mode and shortest spin waves wavelength. For clear observation of the fastest exchange magnons mode, we present the spectra with the field range from 0 mT to 60 mT. As shown in Fig. S2(b), the transmission spectra S_{21} of the 50 nm wide Co nanowire device, from which one can observe the signal about 26.85 GHz pointed by the white arrow when the magnetic field is zero. The dispersion of dipolar-exchange magnons at zero field is present in (Fig. S2(c)), the black point on the red curve is the observed spin-wave resonance frequency extracted from spectra. After calculation, one can calculate that the wavevector of spin waves is about 130 rad μm^{-1} corresponding to 48 nm wavelength.

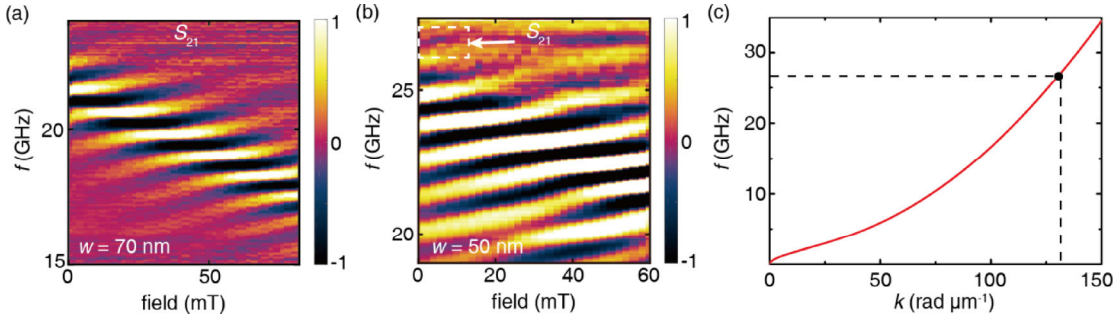

Figure S2 The color-coded spectra and dispersion of the observation of exchange spin waves with wavelength down to 48 nm. (a), (b), Transmission spectra S_{21} of the 70 nm and 50 nm wide Co nanowire device, the shortest wavelength exchange magnons mode is pointed by the white arrow. (c) The dispersion when the magnetic field is zero for calculating the wavelength from the results in Fig. S2(b).

Theory model of spin-wave chiral dynamics

Here, we formulate the theory of chiral spin pumping and (long-range) chiral interaction between ferromagnetic nanowires mediated by unidirectionally excited spin waves in the ferromagnetic film. We focus on the experimental observables, such as the additional damping of Co magnon and the microwave transmission spectra.

We consider the effectively one-dimensional model in Fig. S3 with two sufficiently long magnetic nanowires (thickness s_{Co} and width w) on the top of a thin YIG film. The distance between the nanowires $d \gg w$. The nanowires are excited and detected by local metal stripline antennas with small rectangular cross section of widths w_0 and thicknesses s_0 and uniform AC electric current distributions.

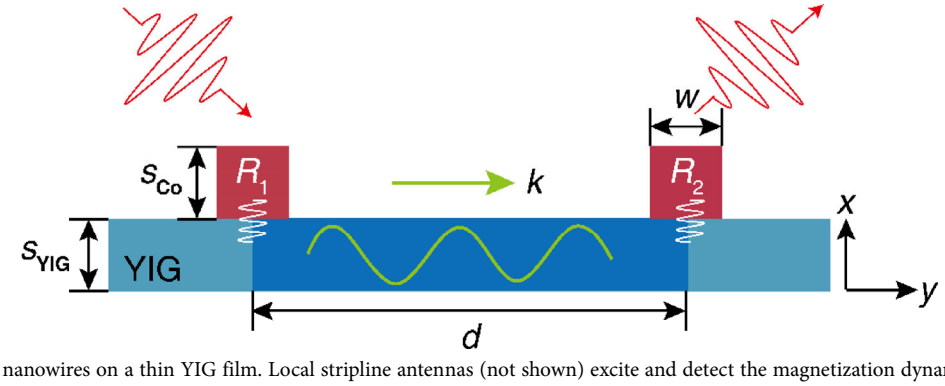

Figure S3 Two Co nanowires on a thin YIG film. Local stripline antennas (not shown) excite and detect the magnetization dynamics in the nanowires. The green arrow indicates the unidirectionally excited magnon current in the film.

Theory of stripline magnetic field distribution

A stripline carrying a harmonic current source $\mathbf{J}(t) = \mathbf{J}(\omega)e^{-i\omega t}$ generates the vector potential

$$\boldsymbol{A}(\boldsymbol{r},\omega) = \frac{\mu_0}{4\pi}\int d\boldsymbol{r}'\boldsymbol{J}(\boldsymbol{r}',\omega)\frac{e^{ik|\boldsymbol{r}-\boldsymbol{r}'|}}{|\boldsymbol{r}-\boldsymbol{r}'|}, \tag{S1}$$

where $k = \omega / c$ and the magnetic field

$$\boldsymbol{H}(\boldsymbol{r}) = \nabla \times \frac{\mathbf{A}(r)}{\mu_0} = \frac{\left(\partial_y A_z, -\partial_x A_z, 0\right)}{\mu_0}. \tag{S2}$$

The current is non-zero in the antenna for $0<x<s_0$ and $-\frac{w_0}{2}<y<\frac{w_0}{2}$, which leads to the Fourier components of the magnetic field

$$H_x(x,k_y,\omega)=i\frac{\boldsymbol{J}(\omega)}{4\pi}\mathcal{F}(s_0,w_0)\frac{k_y}{\sqrt{k_y^2-k^2}}e^{\sqrt{k_y^2-k^2}x},$$
$$H_y(x,k_y,\omega)=-\frac{\boldsymbol{J}(\omega)}{4\pi}\mathcal{F}(s_0,w_0)e^{\sqrt{k_y^2-k^2}x}, \tag{S3}$$

with form factor

$$\mathcal{F}(s_0,w_0)=\frac{4}{k_xk_y}e^{ik_x\frac{s_0}{2}}\sin\left(k_x\frac{s_0}{2}\right)\sin\left(k_y\frac{w_0}{2}\right). \tag{S4}$$

At microwave frequencies $\omega/2\pi\sim 10\text{GHz}$, $k=\omega/c\sim 200\text{radm}^{-1}$ and wavelength $\lambda=2\pi/k\sim 3$ cm. Since the wavelengths of the excited spin waves at this frequency are much smaller (see below), we are in the near-field limit. The Fourier component of the evanescent magnetic field $H_x\rightarrow i\text{sgn}(k_y)H_y$ is circularly polarized in the momentum space with a sign locked to its linear momentum.

The spatial distribution of the stripline magnetic field is the real part of the inverse Fourier transform ($k\equiv k_y$),

$$\mathbf{H}_\alpha(x,y,t)=\sum_k e^{iky-i\omega t}\mathbf{H}_\alpha(x,k). \tag{S5}$$

We plot a snapshot of the spatial distribution of $\boldsymbol{H}(x,0,t)$ by a stripline antenna with $s_0=120$ nm and $w_0=200$ nm in Fig. S4, noting that H_y decays faster than H_x. The latter is seen to be still significant at a distance of 1.5 μm.

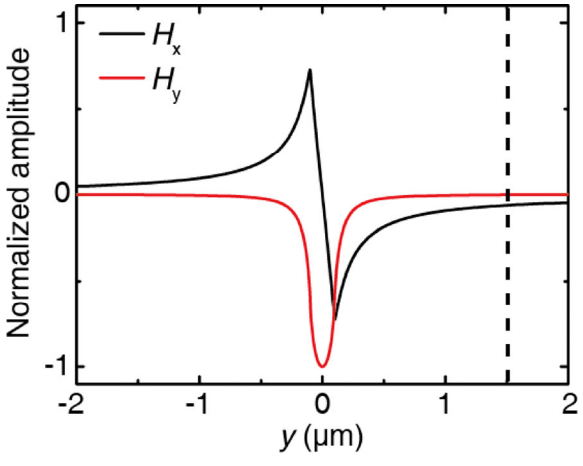

Figure S4 Calculated magnetic-field amplitude excited by a metal stripline antenna with $s_0=120$ nm and $w_0=200$ nm, carrying an AC current with frequency $\frac{\omega}{2\pi}=10$ GHz. The field components are normalized by the maximum value of H_y.

Theory of magnon coupling by dipolar interaction

The magnetization $\tilde{\text{M}}_l$ of the l-th magnetic wire couples with the dipolar field h from the magnetization dynamics of the film $\boldsymbol{M}$ by the Zeeman interaction

$$\hat{H}_{int}=-\mu_0\int_0^{s_{\text{YIG}}}dxd\boldsymbol{\rho}\tilde{M}_{l,\beta}(x,\boldsymbol{\rho})h_\beta(x,\boldsymbol{\rho}), \tag{S6}$$

where μ_0 is the vacuum permeability and we use the summation convention over repeated Cartesian indices $\beta=\{x,y,z\}$. The magnetizations $\tilde{\boldsymbol{M}}_l\|\hat{\boldsymbol{z}}$ are anti-parallel to $\boldsymbol{M}\|-\hat{\boldsymbol{z}}$. We focus on the linear regime and disregard magnon interactions in the film. The magnetization operators in the magnetic wires and film are expanded by the magnon mode amplitudes and operators,

$$\hat{M}_\alpha(r)=-\sqrt{2M_s\gamma\hbar}\sum_k\left(m_\alpha^{(k)}(x)e^{iky}\hat{\alpha}_k+\text{H.c.}\right),$$
$$\hat{\tilde{M}}_{\alpha,l}(r)=-\sqrt{2\tilde{M}_{s,l}\gamma\hbar}\left(\tilde{m}_{l,\alpha}^K(\boldsymbol{r})\hat{\beta}_l+\text{H.c.}\right), \tag{S7}$$

where M_S and $\tilde{M}_{S,l}$ are the saturated magnetizations of film and nanowire, $-\gamma$ is the electron gyromagnetic ratio, $m_\alpha^{(k)}(x)$ and $\tilde{m}_{l,\alpha}^K(\boldsymbol{r})$, respectively, represent the amplitude of the spin waves and Kittel modes, and $\hat{\alpha}_k$ and $\hat{\beta}_l$ denote the magnon operators in the film and nanowire. The l-th nanowire centered at $\boldsymbol{r}_l=R_l\hat{\boldsymbol{y}}$ feels the dipolar field

$$h_\beta(\boldsymbol{r})=-\frac{1}{4\pi}\partial_\beta\partial_\alpha\int d\boldsymbol{r}'\frac{M_\alpha(\boldsymbol{r}')}{|\boldsymbol{r}-\boldsymbol{r}'|}. \tag{S8}$$

The Hamiltonian then reads:

$$\frac{\hat{\mathcal{H}}}{\hbar}=\sum_l \omega_{0,l}\hat{\beta}_l^{\dagger}\hat{\beta}_l+\sum_k \omega_k\hat{\alpha}_k^{\dagger}\hat{\alpha}_k+\sum_l\sum_k\left(g_{k,l}e^{-ikR_l}\hat{\beta}_l\hat{\alpha}_k^{\dagger}+g_{k,l}^{*}e^{ikR_l}\hat{\beta}_l\hat{\alpha}_k\right), \tag{S9}$$

where the coupling constants

$$g_{k,l}=F_l(k)\left(m_x^{(k)*},m_y^{(k)*}\right)\begin{pmatrix}|k| & ik\\ ik & -|k|\end{pmatrix}\begin{pmatrix}\tilde{m}_{l,x}^{\mathrm{K}}\\ \tilde{m}_{l,y}^{\mathrm{K}}\end{pmatrix}, \tag{S10}$$

are real $g_{k,l}=g_{k,l}^{*}$ and the form factor

$$F_l(k)=-2\mu_0\gamma\sqrt{M_{\mathrm{S}}\tilde{M}_{\mathrm{S}}/\Lambda}\left(1-e^{-|k|s_{\mathrm{Co}}}\right)\left(1-e^{-|k|s_{\mathrm{YIG}}}\right)\frac{1}{k^3}\sin\left(\frac{kw}{2}\right). \tag{S11}$$

The length Λ of the magnetic nanowire is sufficiently long to warrant the two-dimensional treatment. Perfect chiral coupling corresponds to $g_{-|k|}=0$, which is realized when the spin waves are circularly polarized, i.e. with $m_y^{(k)}=-im_x^{(k)}$ (for $\mathbf{M}\,||\,-\hat{\mathbf{z}}$). The chirality of the dipolar coupling can be understood from the distribution of the dipolar field: the dipolar field generated by the right (left) moving spin waves vanishes below (above) the film and precesses oppositely to the magnetization.

With $\mu_0 M_{\mathrm{S}}=0.177$ T for YIG and $\mu_0\tilde{M}_{\mathrm{S}}$ =1.67 T for Co, we plot $|g_k|^2$ for spin waves in YIG of thickness 20 nm and a Co nanowire of thickness s_{Co} = 30 nm and w = 60 nm in Fig. S5. The coupling is indeed chiral and shows minima for spin waves with particular momentum $k=2n\pi/w$, where $n\geq 0$ is an integer. The coupling is strongest for $0<k\lesssim\pi/w$. In the following, we take unit length of the nanowire such that Λ = 1.

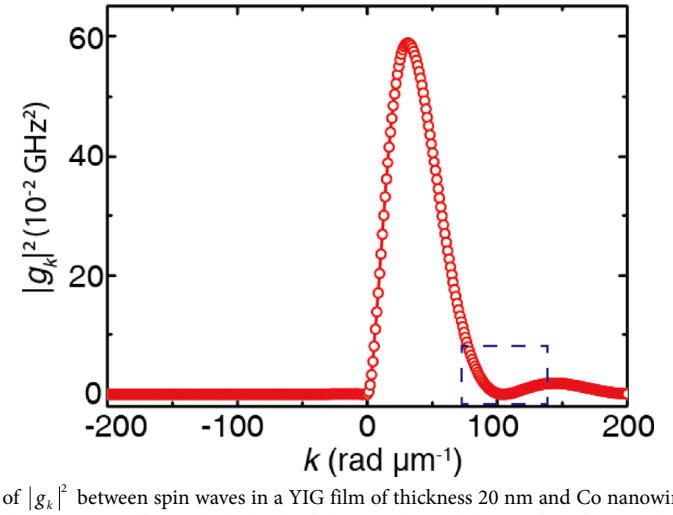

Figure S5 Momentum dependence of $|g_k|^2$ between spin waves in a YIG film of thickness 20 nm and Co nanowire with $s_{\mathrm{Co}}=30$ nm and $w=60$ nm. A zoom-in of this figure (blue box) is shown in Fig. 4(f), in which the shaded area indicated the wavelength interval extracted from the experiments of Fig. 4 in the main text.

Theory of magnon damping by chiral spin pumping

With one magnetic wire centered at the origin R = 0 and the input of microwave expressed by the operator $\hat{p}_{in}$, the magnon equations of motion read

$$\begin{aligned}\frac{d\hat{\beta}(t)}{dt}&=-i\omega_0\hat{\beta}(t)-i\sum_k g_k\hat{\alpha}_k(t)-\left(\frac{\kappa}{2}+\frac{\kappa_p}{2}\right)\hat{\beta}(t)-\sqrt{\kappa_p}\hat{p}_{in}(t),\\ \frac{d\hat{\alpha}_k(t)}{dt}&=-i\omega_k\hat{\alpha}_k(t)-ig_k\hat{\beta}(t)-\frac{\kappa_k}{2}\hat{\alpha}_k(t).\end{aligned} \tag{S12}$$

Here, $\alpha_{\mathrm{G}}=\kappa/(2\omega)$ is the intrinsic (Gilbert) damping of the Kittel modes in the nanowire, κ_p is the radiative damping induced by the microwave photons $\hat{p}_{in}$, i.e., the coupling of the nanowire to the microwave source, and κ_k denotes the intrinsic (Gilbert) damping of magnons with momentum k in the films, ω_0 is the frequency of the Kittel mode of wire. In frequency space, we obtain

$$\begin{aligned}\hat{\alpha}_k(\omega)&=g_kG_k(\omega)\hat{\beta}(\omega),\\ \hat{\beta}(\omega)&=\frac{-\sqrt{\kappa_p}}{-i(\omega-\omega_0)+\frac{\kappa+\kappa_p}{2}+i\sum_k g_k^2G_k(\omega)}\hat{p}_{in}(\omega),\end{aligned} \tag{S13}$$

where $G_k(\omega)=\dfrac{1}{(\omega-\omega_k)+\frac{i\kappa_k}{2}}$ is the magnon Green function. The chiral coupling $g_{-|k|}=0$ only excites spin waves with

positive momentum, i.e., a unidirectionally excited magnon current. An imaginary part of the magnon self-energy indicates additional damping. In the on-shell approximation with $\omega \to \omega_0$

$$\sigma_k(\omega_0) = -\mathrm{Im}\left(\sum_k |g_k|^2 G_k(\omega_k)\right) = \sum_k |g_k|^2 \frac{\frac{\kappa_k}{2}}{(\omega_0-\omega_k)^2+\left(\frac{\kappa_k}{2}\right)^2} \to \frac{1}{2}\frac{|g_k|^2}{v_{k_r}}, \tag{S14}$$

where $\omega_{k_r} = \omega_0$, v_{k_r} is the magnon group velocity.

We compute the additional damping by spin waves pumping for a Co nanowire of thickness 30 nm and different widths, disregarding any interface exchange. We use the magnetizations $\mu_0 M_S = 0.177$ T for YIG and 1.67 T for Co. The intrinsic Gilbert damping coefficient of Co wire is taken to be $\alpha_G = 0.01$. Figure S6 are the plots of the additional σ and intrinsic broadening $\kappa_{Co}/2 = \alpha_G \omega_{Co}$ of the wire Kittel magnon as a function of the external magnetic field.

$$\Delta\omega = 2\left(\sigma_k + \frac{\kappa_{Co}}{2}\right). \tag{S15}$$

σ_k depends on the wire width (and thickness) via the form factor (see Fig. S6). By the magnetic field, the additional damping can be tuned to equal the intrinsic one.

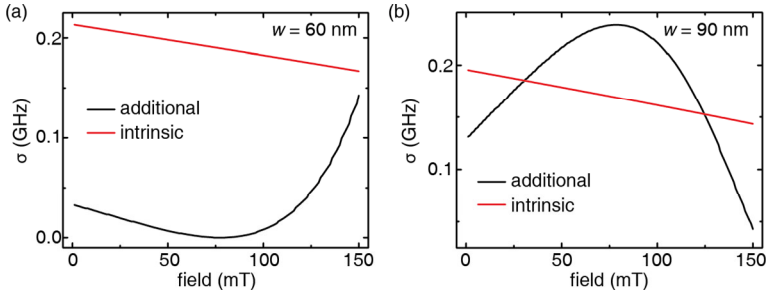

Figure S6 Additional broadening σ_k and intrinsic broadening $\kappa_{Co}/2$ of the wire magnon as a function of the applied magnetic field. The effective damping can be measured by the line broadening of FMR of the microwave reflection $S_{11}(\omega)$.

Theory of phase relation between nanowires

We now consider two magnetic nanowires located at $\boldsymbol{r}_1 = R_1\hat{\boldsymbol{y}}$ and $\boldsymbol{r}_2 = R_2\hat{\boldsymbol{y}}$ that act as transducers for microwaves emitted and detected by local striplines.

When the Kittel magnon at R_1 and R_2 are expressed by the operators $\hat{\beta}_L$ and $\hat{\beta}_R$, respectively, the equations of motion of nanowire and film magnetization read

$$\begin{aligned}
\frac{d\hat{\beta}_L(t)}{dt} &= -i\omega_{0,L}\hat{\beta}_L(t) - i\sum_k g_{k,L}e^{ikR_1}\hat{\alpha}_k(t) - \left(\frac{\kappa_L}{2}+\frac{\kappa_{p,L}}{2}\right)\hat{\beta}_L(t) - \sqrt{\kappa_{p,L}}\hat{p}_{in}^{(L)}(t),\\
\frac{d\hat{\beta}_R(t)}{dt} &= -i\omega_{0,R}\hat{\beta}_R(t) - i\sum_k g_{k,R}e^{ikR_2}\hat{\alpha}_k(t) - \frac{\kappa_R}{2}\hat{\beta}_R(t),\\
\frac{d\hat{\alpha}_k(t)}{dt} &= -i\omega_k\hat{\alpha}_k(t) - ig_{k,L}e^{-ikR_1}\hat{\beta}_L(t) - ig_{k,R}e^{-ikR_2}\hat{\beta}_R(t) - \frac{\kappa_k}{2}\hat{\alpha}_k(t).
\end{aligned} \tag{S16}$$

In frequency space:

$$\begin{aligned}
\hat{\alpha}_k(\omega) &= G_k(\omega)\left[g_{k,L}e^{-ikR_1}\hat{\beta}_L(\omega) + g_{k,R}e^{-ikR_2}\hat{\beta}_R(\omega)\right],\\
\hat{\beta}_L(\omega) &= \frac{-\sqrt{\kappa_{p,L}}}{-i(\omega-\omega_{0,L}) + \frac{\kappa_L+\kappa_{p,L}}{2} + i\sum_k g_{k,L}^2 G_k(\omega) - f(\omega)}\hat{p}_{in}^{(L)}(\omega),\\
\hat{\beta}_R(\omega) &= \frac{-i\sum_k g_{k,L}g_{k,R}G_k(\omega)e^{ik(R_2-R_1)}}{-i(\omega-\omega_{0,R}) + \frac{\kappa_R}{2} + i\sum_k g_{k,R}^2 G_k(\omega)}\hat{\beta}_L(\omega),
\end{aligned} \tag{S17}$$

where

$$f(\omega) \equiv -\frac{(\sum_k g_{k,L}g_{k,R}G_k(\omega)e^{ik(R_1-R_2)})(\sum_k g_{k,L}g_{k,R}G_k(\omega)e^{ik(R_2-R_1)})}{-i(\omega-\omega_{0,R}) + \frac{\kappa_R}{2} + i\sum_k g_{k,R}^2 G_k(\omega)}. \tag{S18}$$

For perfect chiral coupling $f(\omega)$ vanishes by the absence of backaction.

The Eq. S19 gives the phase relation between $\hat{\beta}_R$ and $\hat{\beta}_L$ when the left nanowire is excited. When the two nanowires have the same parameters $g_{k,L} = g_{k,R} = g_k$. Then, at the FMR $\omega \to \omega_{0,L} = \omega_{0,R}$,

$$\hat{\beta}_R(\omega_0) = -\chi(\omega_0) e^{ik_r(R_2-R_1)} \hat{\beta}_L(\omega_0), \tag{S19}$$

where

$$\chi(\omega_0) = \frac{2\sigma_k(\omega_0)}{\frac{\kappa_R}{2} + \sigma_k(\omega_0)}, \tag{S20}$$

modulates the excited magnon amplitude. This corresponds to a phase shift

$$\Delta\phi = \pi + k_r(R_2 - R_1), \tag{S21}$$

between the two nanowires.

Spin-wave dispersion at different fields

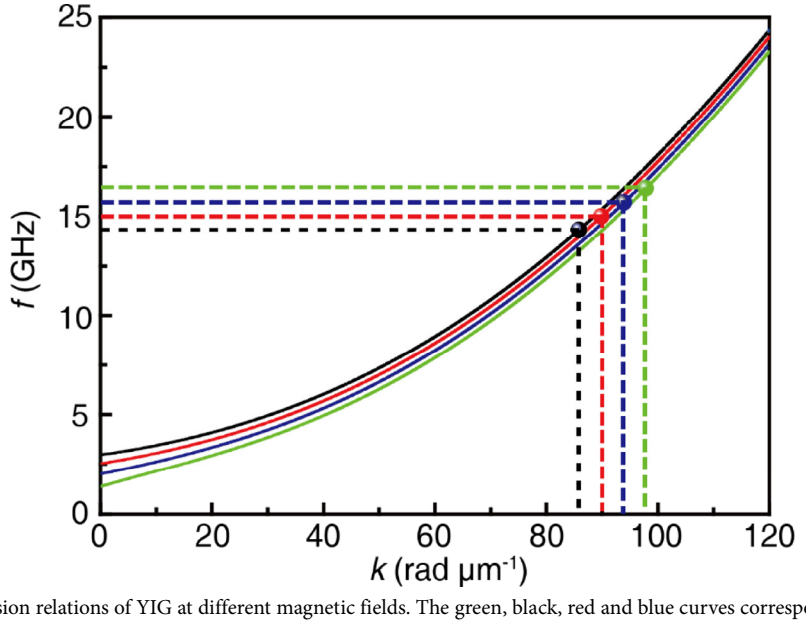

Figure S7 Spin wave dispersion relations of YIG at different magnetic fields. The green, black, red and blue curves correspond to 13 mT, 26 mT, 38.5 mT and 51 mT, respectively. The four data points marked in the figure correspond to the four spin-wave intensity peaks in Fig. 3(d) in the main text.

The dipolar-exchange spin wave dispersion in the Damon-Eshbach configuration reads:

$$f = \frac{\gamma}{2\pi}\left[\left(\mu_0 H + A\mu_0 M_S k^2\right)\left(\mu_0 H + A\mu_0 M_S k^2 + \mu_0 M_S\right) + \frac{\left(\mu_0 M_S\right)^2}{4}\left(1 - e^{-2kt}\right)\right]^{\frac{1}{2}}, \tag{S22}$$

where $|\gamma/2\pi|$ is an absolute gyromagnetic ratio of YIG with 28 GHz T^{-1}, μ_0 is the vacuum permeability, $A = 3\times10^{-12}\,\mathrm{cm}^2$ the exchange stiffness constant, and $\mu_0 M_S = 0.18$ T is the saturation magnetization (see Fig. S1) of the film with 20 nm-thick. Here the wavenumber k is large, the exchange term $A\mu_0 M_S k^2$ dominates and the spin-wave dispersion relation is quadratic. Figure S7 shows four dispersion curves, corresponding to the applied field $\mu_0 H$ of 13 mT, 26 mT, 38.5 mT and 51 mT. Four points are marked in the figure with different wavenumbers, corresponding to the peaks in Fig. 3(d) in the main text. We find a wave vector variation Δk between the neighbouring wavenumbers of 4 rad μm^{-1}, which gives a spin wave phase shift of 6.0 rad.

Scanning electron microscope (SEM) images of the devices

The SEM images in Figs. S8(a)-8(f) show Co nanowires on top of YIG that vary in width from 50 to 220 nm. The asymmetric device width of 60 nm and 80 nm shows in Fig. S8(g). The Co nanowires are fabricated on YIG waveguides and the center-to-center distance d is 1.5 μm. The SEM image of antennas on Co nanowires is shown in Fig. S8(h), with the width of antennas around 200 nm. The scale bars are both 500 nm in Fig. S8.

Coupling strength modulated by the nanowire width and spin-wave wavenumber

The equation of g_k in the main text involves the coupling strength between the FMR modes of two Co nanowires on a YIG film that in our model depends on wave number k and the width of the nanowire w. In the main text, we discuss the relative coupling strength as a function of the spin-wave wavelength for 60 nm wide Co nanowires for different propagation distances. Here, we show the S_{21} transmission spectra, the spectrum along the Co nanowire resonance (red dashed lines in S_{21}) and the relative coupling strength (or form factors) as a function of the spin-wave wavelength for various samples.

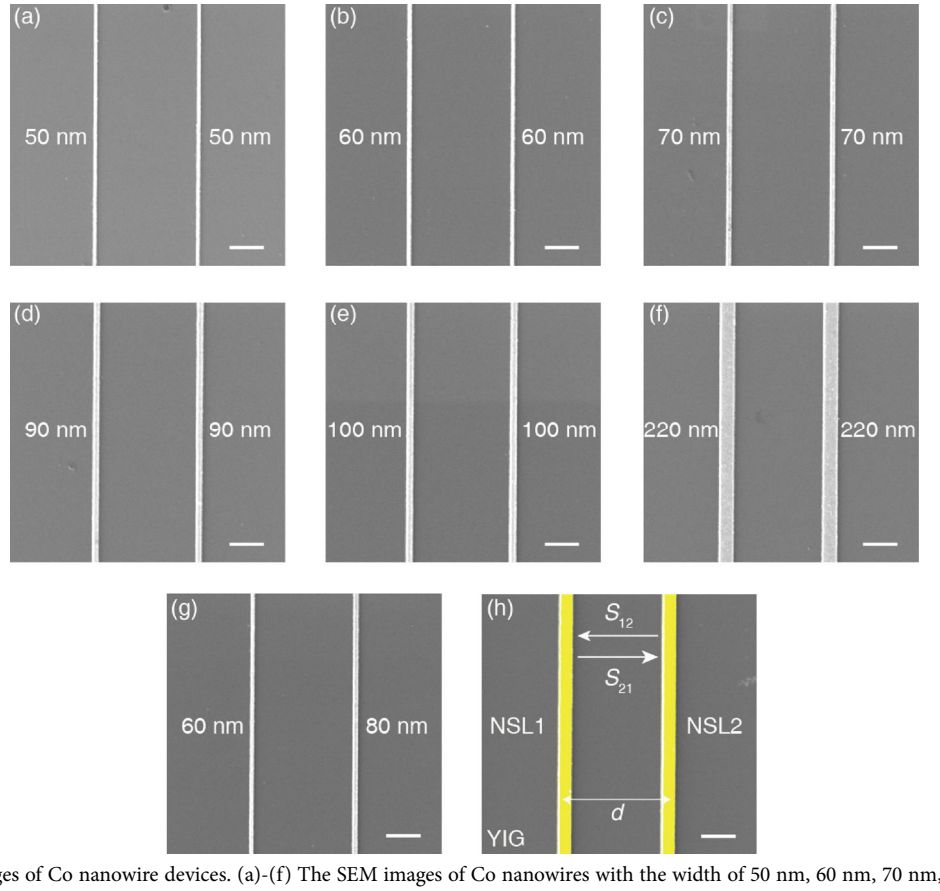

Figure S8 SEM images of Co nanowire devices. (a)-(f) The SEM images of Co nanowires with the width of 50 nm, 60 nm, 70 nm, 90 nm, 100 nm, and 220 nm. (g) The SEM images of the different widths Co nanowires device with the width of 60 nm and 80 nm. (h) Two antennas (yellow) with width of about 200 nm are fabricated on the Co nanowires. The center-to-center distance d between the wires and antennas is 1.5 μm. The scale bar in all images is 500 nm.

Fig. S9(a) shows the transmission spectra S_{21} of the sample with different wire widths $w \neq w'$, excited on the w = 60 nm side and detected on the w' = 80 nm side. The transmission decreases with frequencies, which is consistent with the form factor of g_k in the main text. The relative Co-Co coupling strength of this case reads $(g_k / g_0) \times (g'_k / g'_0)$ and is plotted in Fig. S9(c) as a function of wavelength λ. The blue background emphasizes the wavelength range from 56.8 nm to 70.1 nm, which is important for the interpretation of the spectrum in Fig. S9(b).

Then, for the same width of two Co nanowires device, S_{21} spectra of 90 nm wide is presented in Fig. S9(d), in which the red dashed line is along the Co nanowire resonance frequency, 20.1 GHz at 0 mT (spin-wave wavelength is about 56.5 nm) and 17.1 GHz at 64 mT (spin-wave wavelength is about 66.1 nm). Then, as shown in the Fig. S9(e), the lineplot spectrum extracted along the red dashed line in S_{21}, where the blue dashed line is a guide to the eye. One could find that the tendency of the lineplot along the red dashed line is consistent with the tendency of relative coupling strength from 56.5 nm to 66.1 nm as presented in Fig. S9(f). As shown in Fig. S9(g)-9(i), we also calculate the relative coupling strength as a function of wavelength from 61.8 nm to 76.0 nm on 100 nm wide Co nanowire device as presented in Fig. 3 in the main text. The lineplot along the red dashed line in Fig. 3(b) from 17.14 GHz at 0 mT and 13.82 GHz at 60 mT is presented in Fig. 3(d) in the mian text, from which one can find that the tendency of it is consistent with the relative coupling strength. For the 220 nm wide Co nanowire device, as shown in Fig. S9(j)-9(l), the Co nanowire resonance frequency is from 12.64 GHz at 0 mT to 15.57 GHz at 34 mT in the S_{21} spectra (Fig .S9(j)), and relative coupling strength as a function of wavelength from 65.4 nm to 77.8 nm (Fig .S9(l)). These measurements unequivocally present the coupling between the FMR mode of Co wire and the spin-wave mode of YIG film.

Micromagnetic simulations of chiral coupling and chiral spin waves

Micromagnetic simulations based on the public object-oriented micromagnetic framework (OOMMF, http://math.nist.gov/oommf) confirm and help to understand the chiral coupling between Co nanowire and YIG film. The YIG film has the dimensions 20 nm × 2 μm × 2 μm (xyz) and the Co nanowire with dimensions 20 nm × 200 nm × 2 μm (xyz) is along the z axis directly on top of the center of the YIG film. The saturation magnetizations $\mu_0 M_s$ = 1.5 T and 0.175 T and the exchange constant are 13×10^{-12} J m^{-1} and 3.7×10^{-12} J m^{-1} for the Co nanowire and YIG film, respectively. The interlayer exchange coupling is disregarded. The Gilbert damping of the YIG film $\alpha = 8 \times 10^{-5}$. An external field of -200 mT in the z direction is first applied to align the magnetization of Co and YIG into the same direction. Applying subsequently a positive static magnetic field of 20 mT, we establish a stable AP state. An oscillating external field of $\mu_0 H_{ex} = 0.2\text{mT} \times \sin(2\pi f t)$ is applied on the Co nanowire with the frequency f = 15 GHz. The spatial map of the YIG film magnetization after 1 ns is shown in Fig. S10(a) where the region of Co is marked on the figure. The directionality of the exchange spin waves is evident and caused by the chiral magnetodipolar coupling between the Co nanowire and YIG film. A lineplot extracted from Fig. S10(a) is shown in Fig. S10(b).

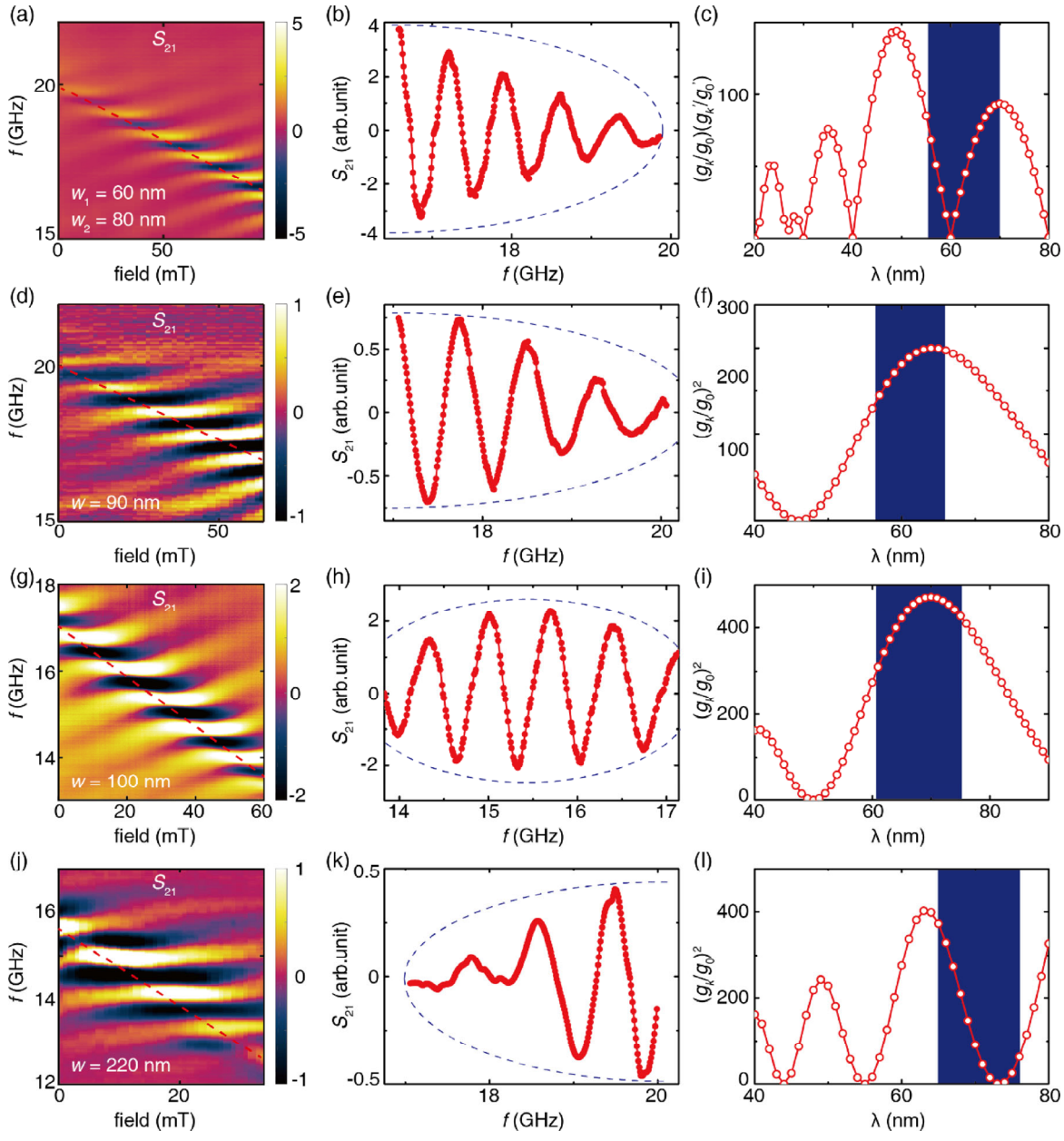

Figure S9 Coupling between Co Kittel modes via spin waves as a function of the nanowire width w and wavelength λ. (a) The transmission spectra S_{21} close to the Co nanowire resonance frequency. (b) A cut of S_{21} along the red-dashed line of (a), and the relative coupling strength as a function of wavelength when the exciting wire is 60 nm and the detector 80 nm wide. (d), (g), (j), The transmission spectra S_{21} when both wires are 90 nm (Fig. S9(d)), 100 nm (Fig. S9(g)), and 220 nm (Fig. S9(j)) wide. (e), (h), (k), Along the resonance frequency of Co nanowire (the red dashed line in S_{21}), the lineplot spectra are extracted and present in Fig. S9(e) (90 nm wide), Fig. S9(h) (100 nm wide), Fig. S9(k) (220 nm wide). The blue dashed lines in the lineplot spectra indicate a guide to the eye. Base on the form factor of g_k in the main text, we calculate the relative coupling strength as a function of the spin-wave wavelength. The blue region is the range of spin-wave wavelength extracted from the transmission spectra.

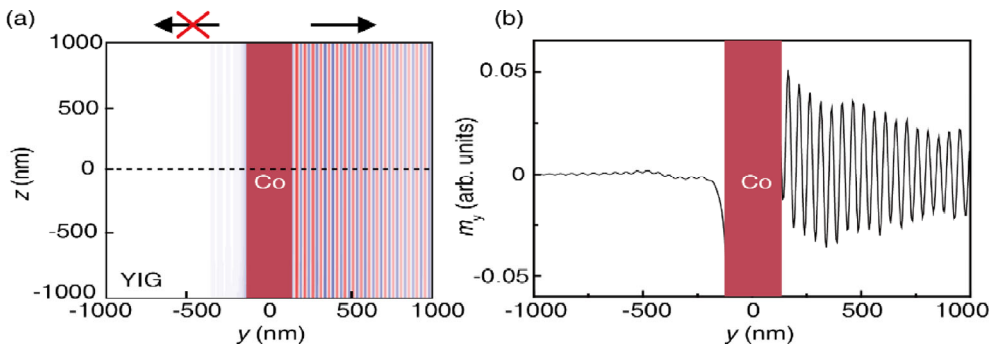

Figure S10 Exchange spin waves in YIG film excited by the magnetic resonance of a Co wire contact. (a) The spatial map of a snapshot of the y-component of exchange spin waves 1 ns after switching on the Co FMR with frequency $f = 15$ GHz. The region covered by the Co nanowire is marked in the figure. (b) Lineplot extracted from (a) at $z = 0$ nm.

Micromagnetic simulations of spin-wave coupling between two nanomagnets

Next, we simulate a sample with two identical Co nanowires with dimensions of 20 nm × 100 nm × 90 μm (*xyz*) along the *z* axis on top of a YIG thin film with dimensions of 20 nm ×3.5 μm × 90 μm (*xyz*). The Co nanowires, Co1 and Co2, have a center-to-center distance of 1.5 μm. An external field of -200 mT is first applied along *z* to align the magnetizations of Co and YIG. Next, we establish an equilibrium state by a positive static magnetic field along *z* that favors the AP state. An ac magnetic field pulse of the form $\mu_0 H_{ex} = 0.2\text{mT} \times \text{sinc}(2\pi ft)$ is applied in the *y* direction on Co1 only. The Fourier transform of the sinc function is rectangular with high-frequency cut-off at *f*. The numerical time step is 20 ps and result are recorded over 4 ns. The middle image in Fig. S11 is a fast Fourier transform (FFT) of the computed magnetization amplitude $m_y(t)$ of the Co2 for static applied fields from 0 mT to 50 mT. The obtained spectra can be compared with the experimental steady state transmission spectra S_{21}. The clear resonance mode is the evidence for coupling of nanomagnets via exchange spin waves. In order to obtain the phase information, we apply a periodic AC magnetic field $\mu_0 H_{ex} = 0.2\text{mT} \times \sin(2\pi ft)$ in the *y* direction to Co1 with variable *f*. For an external field of 29.4 mT and *f* =15.25 GHz, the phase shift between the Co1 and Co2 dynamics vanishes ΔΦ =0°. By modulating the applied field and frequency, we show in Fig. S11 that the phase difference can be tuned from 0° to 315°.

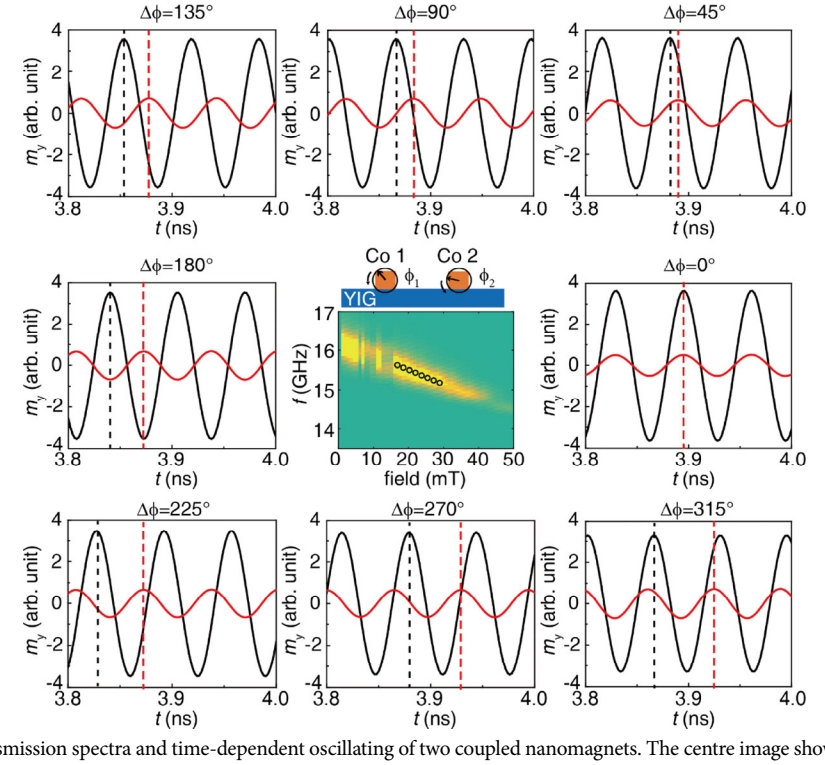

Figure S11 Simulated transmission spectra and time-dependent oscillating of two coupled nanomagnets. The centre image shows the simulated transmission spectra of the Co2 from 0 mT to 50 mT. The time-dependent oscillations of the Co1 and Co2 with the phase shift ΔΦ from 0° to 315° are shown from 3.8 ns to 4.0 ns with the applied field of 29.4 mT (ΔΦ =0°), 27.3 mT (ΔΦ =45°), 25.3 mT (ΔΦ =90°), 23.3 mT (ΔΦ =135°), 21.3 mT (ΔΦ =180°), 19.3 mT (ΔΦ =225°), 17.3 mT (ΔΦ =270°) and 15.3 mT (ΔΦ =315°), respectively. These eight fields are marked in the transmission spectra by black circles.

Micromagnetic simulations of crosstalk coupling between two nanomagnets

Next, we discuss the crosstalk coupling between two nanomagnets. A periodic AC magnetic field is applied in the *y* direction to Co1 with variable *f*. The external field of 29.4 mT and *f* =15.25 GHz are set and the phase shift between the Co1 and Co2 vanishes. The spatial map is shown in Fig. S12(a) and the Co2 is coupled by exchange spin waves in YIG. In Fig. S12(b), same AC magnetic field is applied to Co2 and the exchange spin waves cannot reach Co1 due to the chiral coupling. The time-dependent oscillations in Co1 (excited by Co2) and Co2 (excited by Co1) is shown in Fig. S12(c) and the coupling via chiral spin waves is about 6.3 times (close to experiments) stronger than that of crosstalk. The origin of the crosstalk may come from the direct dipolar coupling between two nanomagnets.

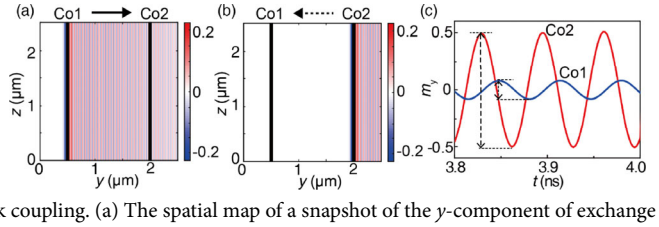

Figure S12 Simulated of the crosstalk coupling. (a) The spatial map of a snapshot of the *y*-component of exchange spin waves in YIG 2 ns after switching on the Co1 FMR with frequency $f = 15.25$ GHz. The external field is applied at 29.4 mT. The region covered by the Co nanowire is marked by black stripes in the figure. (b) The spatial map of a snapshot of the *y*-component of exchange spin waves in YIG 2 ns after switching on the Co2 FMR. (c) The time dependent oscillations of Co1 (excited by Co2) and Co2 (excited by Co1).

Theory of scattering matrix

The phase relation Eq. S17 affects the microwaves transmission with excitation (input) at R_1 and the detection (output) at R_2 which we calculate by the input-output theory. The excitation of the left nanowire propagates to the right one by the spin waves in the film. The observed microwave output of the left and right nanowires inductively detected by the stripline antennas are denoted by $\hat{p}_{out}^{(L)}(\omega)$ and $\hat{p}_{out}^{(R)}(\omega)$ with input-output relations

$$\begin{aligned}\hat{p}_{out}^{(L)}(\omega) &= p_{in}^{(L)} + \sqrt{\kappa_{p,L}}\hat{\beta}_L(\omega),\\ \hat{p}_{out}^{(R)}(\omega) &= \sqrt{\kappa_{p,R}}\hat{\beta}_R(\omega),\end{aligned} \tag{S23}$$

where $\kappa_{p,R}$ is the additional radiative damping induced by the detector. The microwave reflection (S_{11}) and transmission (S_{21}) amplitudes become

$$\begin{aligned}S_{11}(\omega) &= \frac{\hat{p}_{out}^{(L)}}{\hat{p}_{in}^{(L)}} = 1 - \frac{\kappa_{p,L}}{-i(\omega-\omega_{0,L}) + \dfrac{\kappa_L+\kappa_{p,L}}{2} + i\sum_k g_{k,L}^2 G_k(\omega) - f(\omega)},\\ S_{21}(\omega) &= \frac{\hat{p}_{out}^{(R)}}{\hat{p}_{in}^{(L)}} = [1-S_{11}(\omega)]\sqrt{\frac{\kappa_{p,R}}{\kappa_{p,L}}}\frac{i\sum_k g_{k,L}g_{k,R}G_k(\omega)e^{ik(R_2-R_1)}}{-i(\omega-\omega_{0,R}) + \dfrac{\kappa_R}{2} + i\sum_k g_{k,R}^2 G_k(\omega)}.\end{aligned} \tag{S24}$$

Similarly, we obtain S_{12} and S_{22} when excite the second wire and detect the response at the first wire (note $f(\omega)=0$ by chiral interaction):

$$\begin{aligned}S_{22}(\omega) &= 1 - \frac{\kappa_{p,R}}{-i(\omega-\omega_{0,R}) + \dfrac{\kappa_R+\kappa_{p,R}}{2} + i\sum_k g_{k,R}^2 G_k(\omega)},\\ S_{21}(\omega) &= [1-S_{22}(\omega)]\sqrt{\frac{\kappa_{p,L}}{\kappa_{p,R}}}\frac{i\sum_k g_{k,R}g_{k,L}G_k(\omega)e^{ik(R_1-R_2)}}{-i(\omega-\omega_{0,L}) + \dfrac{\kappa_L}{2} + i\sum_k g_{k,L}^2 G_k(\omega)}.\end{aligned} \tag{S25}$$

In particular, then from Eq. S17, we find

$$S_{21}(\omega) = [S_{11}(\omega)-1]\sqrt{\frac{\kappa_{p,R}}{\kappa_{p,L}}}\frac{\langle\hat{\beta}_R(\omega)\rangle}{\langle\hat{\beta}_L(\omega)\rangle}, \tag{S26}$$

implying that the transmission spectra can measure the phase relation between the Kittel modes in the right and left nanowires.

Based on the information of the 60 nm wide device in Fig. 4(b) (main text) with propagation distance of 1.5 μm, we theoretically calculate the transmission spectra of this device as shown in Fig. S13, which is consistent with the experiment results. For the parameters used in calculation, we adopt the magnetizations $\mu_0 M_S = 0.177$ T for YIG and 1.67 T for Co. The thickness of YIG film and Co wire is taken to be 20 nm and 30 nm. The exchange stiffness constant is set as $A = 3\times10^{-12}\,\mathrm{cm}^2$.

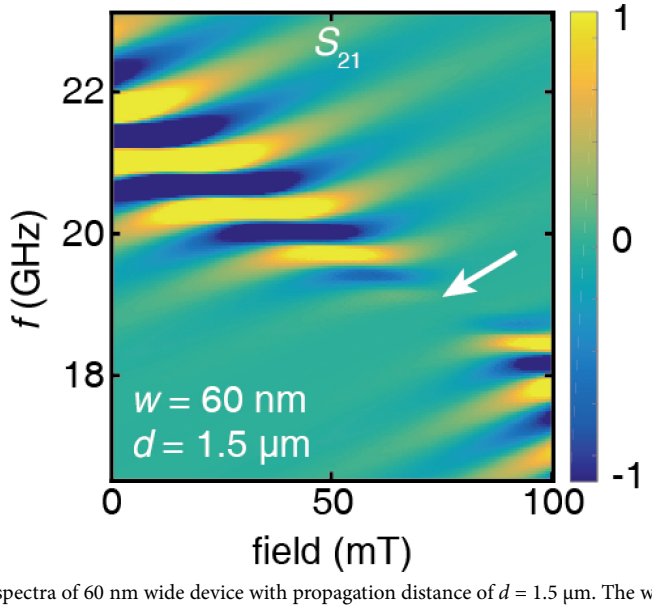

Figure S13 Calculated transmission spectra of 60 nm wide device with propagation distance of d = 1.5 μm. The white arrow shows a valley of amplitude around 19 GHz which is consistent with the observed experiment results in Fig. 4(b) in the main text.

Theory of non-Hermitian coupling

Starting from the equations of motion Eq. S16, the Markov approximation yields

$$\begin{aligned}\frac{d\hat{\beta}_1}{dt} &= -i\omega_1\hat{\beta}_1 + \sum_k \frac{|g_{k,1}|^2}{i(\omega-\omega_k)-\frac{\kappa_k}{2}}\hat{\beta}_1 + \sum_k \frac{g_{k,1}g_{k,2}^*}{i(\omega-\omega_k)-\frac{\kappa_k}{2}}\hat{\beta}_2 + \hat{P}_1,\\ \frac{d\hat{\beta}_2}{dt} &= -i\omega_2\hat{\beta}_2 + \sum_k \frac{|g_{k,2}|^2}{i(\omega-\omega_k)-\frac{\kappa_k}{2}}\hat{\beta}_2 + \sum_k \frac{g_{k,1}^*g_{k,2}}{i(\omega-\omega_k)-\frac{\kappa_k}{2}}\hat{\beta}_1 + \hat{P}_2,\end{aligned} \tag{S27}$$

which are the coupled equation between $\hat{\beta}_1$ and $\hat{\beta}_2$ mediated by the retarded spin waves in the film. $\hat{P}_1$ and $\hat{P}_2$ are noise terms from the local antennas felt by the Kittel magnons. By $g_{k,l} = \tilde{g}_{k,l}e^{ikR_l}$ and with $R_1 > R_2$, we obtain the inter-wire coupling

$$\begin{aligned}\Gamma_{12}(\omega) &\equiv -\int\frac{dk}{2\pi}\frac{g_{k,1}g_{k,2}^*}{i(\omega-\omega_k)-\frac{\kappa_k}{2}} = \frac{1}{v(k_\omega)}\tilde{g}_{k_\omega,1}\tilde{g}_{k_\omega,2}^* e^{ik_\omega(R_1-R_2)},\\ \Gamma_{21}(\omega) &\equiv -\int\frac{dk}{2\pi}\frac{g_{k,1}^*g_{k,2}}{i(\omega-\omega_k)-\frac{\kappa_k}{2}} = \frac{1}{v(k_\omega)}\tilde{g}_{-k_\omega,1}^*\tilde{g}_{-k_\omega,2} e^{ik_\omega(R_1-R_2)},\end{aligned} \tag{S28}$$

and the self-interaction

$$\Gamma_{l=1,2}(\omega) \equiv -\int\frac{dk}{2\pi}\frac{|g_{k,l}|^2}{i(\omega-\omega_k)-\frac{\kappa_k}{2}} \to \frac{1}{2v(k_\omega)}\left(|g_{k_\omega,l}|^2 + |g_{-k_\omega,l}|^2\right). \tag{S29}$$

Here, k_ω is the positive root of $\omega_k = \omega$ and $v(k_\omega)$ the group velocity. In this equation, a simplified scenario is considered where we disregard the spin-wave attenuation $e^{-(R_1-R_2)/l_d}$ in terms of the decay $l_d = v(k_\omega)/(\alpha\omega)$ with $\alpha = 8\times10^{-5}$ being the Gilbert damping of the YIG film as present in Fig. S1. Furthermore, one can estimate that the decay length is about 180μm $\gg |R_1 - R_2| = 1.5$ μm through the experiments of Fig .4 where the group velocity is about 2 km s^{-1}, and the resonance frequency is about 22 GHz. Generally, $|\Gamma_{12}(\omega)| \neq |\Gamma_{21}(\omega)|$ as long as $|g_{k,l}| \neq |g_{-k,l}|$, i.e. when the coupling is non-reciprocal. For two identical nanowires, $|\Gamma_{12}(\omega)| = 2\sigma(\omega)$, i.e., twice of the magnon broadening induced by chiral pumping derived above. In the chiral limit, one of the two couplings vanishes, which means that one magnon affects the other but not the other way around. Such a non-reciprocal interaction cannot be described by a Hermitian Hamiltonian. Even the non-chiral case with $|\Gamma_{12}(\omega)| = |\Gamma_{21}(\omega)|$ is not trivial since the two magnons can hybridize to form acoustic and optical modes, while the dissipative nature of the coupling causes a level attraction rather than the repulsion associated with a coherent coupling.

The effective non-Hermitian Hamiltonian that via the Heisenberg equation of motion recovers the non-reciprocal dynamics reads

$$\frac{\hat{\mathcal{H}}_{\text{eff}}}{\hbar} = \sum_{i=1}^{2}(\omega_l - i\Gamma_l)\hat{\beta}_l^\dagger\hat{\beta}_l - i\Gamma_{12}(\omega)\hat{\beta}_1^\dagger\hat{\beta}_2 - i\Gamma_{21}(\omega)\hat{\beta}_2^\dagger\hat{\beta}_1. \tag{S30}$$

We may divide Eq. S30 into a Hermitian $\hat{\mathcal{H}}_h$ and non-Hermitian $\hat{\mathcal{H}}_{nh}$ part:

$$\hat{\mathcal{H}}_{\text{eff}} = \left(\frac{\hat{\mathcal{H}}_{\text{eff}}}{2} + \frac{\hat{\mathcal{H}}_{\text{eff}}^\dagger}{2}\right) + \left(\frac{\hat{\mathcal{H}}_{\text{eff}}}{2} - \frac{\hat{\mathcal{H}}_{\text{eff}}^\dagger}{2}\right), \tag{S31}$$

$$\begin{aligned}\hat{\mathcal{H}}_h &= \sum_l \omega_l\hat{\beta}_l^\dagger\hat{\beta}_l + i\left(\Gamma_{21}^* - \Gamma_{12}\right)\hat{\beta}_1\hat{\beta}_2 + i\left(\Gamma_{12}^* - \Gamma_{21}\right)\hat{\beta}_1\hat{\beta}_2,\\ \hat{\mathcal{H}}_{nh} &= -i\sum_j \Gamma_l\hat{\beta}_l^\dagger\hat{\beta}_l - i\frac{\Gamma_{12}+\Gamma_{21}^*}{2}\hat{\beta}_1^\dagger\hat{\beta}_2 - i\frac{\Gamma_{12}^*+\Gamma_{21}}{2}\hat{\beta}_1\hat{\beta}_2^\dagger.\end{aligned} \tag{S32}$$

The coupling between magnons has both coherent and dissipative components.